The Annals of Applied Statistics
2024, Vol. 18, No. 2, 1090–1112
https://doi.org/10.1214/23-AOAS1824

NETWORK METHOD FOR VOXEL-PAIR-LEVEL BRAIN CONNECTIVITY ANALYSIS UNDER SPATIAL-CONTIGUITY CONSTRAINTS

BY TONG LU[1,a], YUAN ZHANG[2,b], PETER KOCHUNOV[3,c], ELLIOT HONG[3,d] AND SHUO CHEN[3,e]

[1]*Department of Mathematics, University of Maryland,* [a]*hitonggg@terpmail.umd.edu*
[2]*Department of Statistics, The Ohio State University,* [b]*yzhanghf@stat.osu.edu*
[3]*Maryland Psychiatric Research Center, School of Medicine, University of Maryland,* [c]*pkochunov@som.umaryland.edu,* [d]*pkhong@som.umaryland.edu,* [e]*shuochen@som.umaryland.edu*

Brain connectome analysis commonly compresses high-resolution brain scans (typically composed of millions of voxels) down to only hundreds of *regions of interest* (ROIs) by averaging within-ROI signals. This significant dimension reduction improves computational speed and the morphological properties of anatomical structures; however, it comes at the cost of substantial losses in spatial specificity and sensitivity, especially when the signals exhibit high within-ROI heterogeneity. Oftentimes, abnormally expressed *functional connectivity* (FC) between a pair of ROIs, caused by a brain disease, is primarily driven by only small subsets of voxel pairs within the ROI pair. This article proposes a new network method for the detection of voxel-pair-level neural dysconnectivity with spatial constraints. Specifically, focusing on an ROI pair, our model aims to extract dense subareas that contain aberrant voxel-pair connections while ensuring that the involved voxels are spatially contiguous. In addition, we develop subcommunity-detection algorithms to realize the model, and we justify the consistency of these algorithms. Comprehensive simulation studies demonstrate our method's effectiveness in reducing the false-positive rate while increasing statistical power, detection replicability, and spatial specificity. We apply our approach to reveal: (i) disrupted voxelwise FC patterns related to nicotine addiction between the basal ganglia, hippocampus, and insular gyrus in 3269 participants using UK Biobank data; (ii) voxelwise schizophrenia-altered FC patterns within the salience and temporal-thalamic network in 330 participants in a schizophrenia study. The detected results align with previous medical findings but include improved localized information.

1. Introduction. Statistical network analysis and graph theory have been fundamental in the study of the intricate neural circuits in human brains (the "human connectome") (Bullmore and Sporns (2009), Rubinov and Sporns (2010)). A large body of literature has revealed that the human connectome is a well-organized network, and it exhibits graph properties of intelligent networks such as social networks and the Internet (Bahrami, Laurienti and Simpson (2019), Cao et al. (2014)). Built on graph theory, brain network analysis depicts the brain connectome as a graph in which cortical regions are denoted as nodes and the connections between regions are edges. Under this framework, abundant statistical models have been developed to study the associations between complex neural connections and experimental/clinical conditions (e.g., Fornito, Zalesky and Bullmore (2016), Simpson, Bowman and Laurienti (2013)). These models can help to enhance our understanding of the underlying pathophysiological mechanisms of brain diseases (e.g., Alzheimer's disease and Parkinson's disease) and assist clinical predictions concerning disease diagnosis and treatment selection.

Received January 2023; revised August 2023.
Key words and phrases. Brain connectome, spatial contiguity, voxel-pair-level connectivity, fMRI.

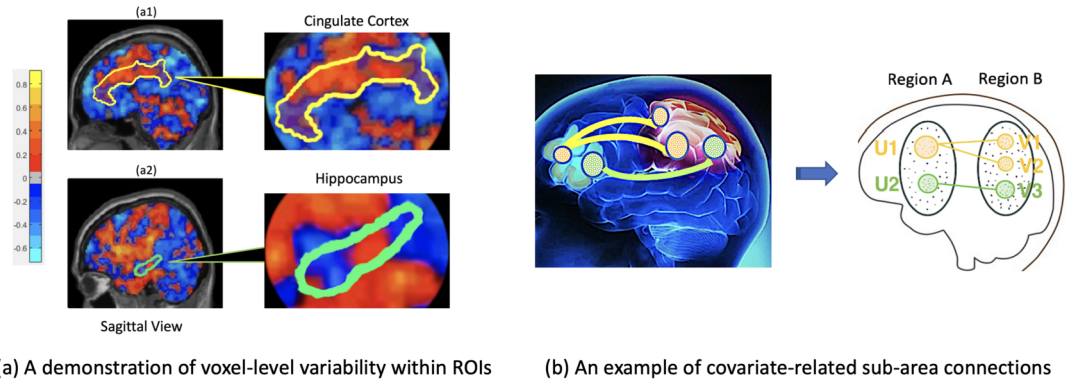

FIG. 1. *(a) shows the heterogeneity of functional connectivity (FC) among intra-ROI voxels through a seed–to-voxel analysis using insula as a seed ROI. While both the cingulate cortex and hippocampus are well-known ROIs, their interior FC with insular varies substantially. (b) shows a simplified example of covariate-related FC of voxel-pairs located in subarea pairs* (U_1, V_1), (U_1, V_2), *and* (U_2, V_3) *within a larger ROI pair (Region A, Region B).*

In brain network studies, regions of interest (ROIs), often considered as basic units of analysis, are equivalent to nodes/vertices in graph theory. The popularity of region-level brain network (RBN) analysis stems from its high anatomical consistency and computational tractability. When a whole-brain connectome is considered, RBN analysis dramatically reduces the search dimensions from trillions ($10^6 \times 10^6$) to thousands ($10^2 \times 10^2$). However, RBN analysis relies on the assumption of signal homogeneity among intra-ROI voxels, which is often violated in reality. When significant intra-ROI heterogeneity is present, RBN analysis can lead to several analytical flaws:

(i) *Variability negligence*. Simply averaging the time series of voxels within an ROI can lead to voxel-level information variability loss (e.g., Figure 1(a)).

(ii) *Spatial specificity loss*. A clinical covariate may alter the ROI-pair connections by disrupting only a small proportion of intra-ROI voxel pairs. In such cases RBN analysis fails to precisely distinguish the localized alteration.

(iii) *Power loss*. The averaging process mixes both significant and nonsignificant voxel-level connections, which often attenuates the effect size and statistical power.

Recently, many brain network studies have shifted focus from RBN analysis to voxel-level network analysis (Loewe et al. (2014), Wu et al. (2013)). Traditional multiple testing methods (e.g., the false-discovery rate (FDR) and the familywise error rate (FWER) control) are not applicable to high-dimensional multivariate voxel pairs since they are unable to take into account anatomical restrictions and inherent systematical patterns of disease-associated voxels in ROIs. Some other existing methods may also have limitations, such as not utilizing rich voxel-level information to complement region-level connectivity characterization, or yielding relatively hard-to-interpret results for various reasons (e.g., underrepresented neurobiological structures or biases in the seed-selection process). Several advanced statistical methods have been proposed to address these limitations. For example, Xia and Li (2017) and Xia and Li (2019) provided localized statistical inference by accounting for the network properties. Chen, Bowman and Mayberg (2016) proposed a Bayesian hierarchical model to identify the voxel-level connectivity patterns associated with clinical covariates and then used the voxelwise functional connectivity (vFC) patterns to infer region-level connections. These novel approaches yield improved inference results and localized specificity. Nonetheless, they are

not directly applicable to our input data of interest (i.e., an $m \times n$ "bi-cluster" rather than an $n \times n$ adjacency matrix), and they do not regulate involved voxels to be spatially contiguous. Unlike RBN analysis, spatial contiguity is crucial for vFC analysis because: (i) it preserves anatomical homogeneity, and it hence preserves the interpretability of the vFC results (Thirion et al. (2006)); (ii) it better controls the FDR and FWER since phenotype-related vFC is often intrinsically linked with the topological structure of the brain connectome (Fan, Han and Gu (2012)).

In this study our goal was to identify altered vFC patterns between spatially contiguous subarea pairs from a larger region pair. More specifically, given a region pair of interest, we sought to extract interior subarea pairs that could maximally cover spatially adjacent covariate-related vFC with well-controlled FDR and FWER values (e.g., Figure 1(b)). Our subarea *extraction* approach is fundamentally distinct from other commonly used brain *parcellation* methods, such as anatomy-based and data-driven approaches (e.g., gradient- or similarity-based mappings) (Craddock et al. (2012), Wig, Laumann and Petersen (2014)); these parcellation methods seek to segment an ROI into different subregions, and every single voxel is assigned to a corresponding subregion. In contrast to parcellation methods in which every voxel is processed, our subarea extraction approach only selects subsets of voxels that are covariate-related and are constrained in spatially contiguous spaces. All other nonselected voxels are considered to be covariate-indifferent. Subarea extraction is more suited to our study because: (i) it is likely that the covariate-related differences across clinical groups may gather in the vFC between a subarea in Region A and an intersection of multiple subareas grouped by the existing parcellation methods in Region B; (ii) it is often found that only a small proportion of voxels in regions A and B are disrupted, and thus a comprehensive parcellation across the entire ROI is not necessary (Cao et al. (2014)).

To achieve the desired subarea extraction and address the limitations discussed above, we propose a new statistical network framework to extract **S**patially **C**onstrained and **C**onnected **N**etworks, hereafter referred to as SCCN. SCCN is a two-step method (Figure 2) focusing between a pair of ROIs, say A and B, that are believed to contain aberrant functional connections caused by a brain disease. In *step 1*, SCCN extracts spatially coherent subarea pairs that maximally contain disease-altered vFC between regions A and B. In *step 2*, we formally test each extracted subarea pair to determine whether it is significantly covariate-associated with multiple testing controls. If no subarea pairs are found to be significant, we then consider the region-pair connectivity as covariate-unrelated. If significant results are seen, the association between the covariate of interest and the ROI-pair connections can be traced down to smaller but much more precise subareas consisting of extracted voxels. These vFC results may provide insights into understanding the latent neurophysiological mechanisms of diseases.

In this paper we show that SCCN provides a consistent estimate for the true community structure in the sense that the error of edge assignments is negligible in large region pairs. We empirically evaluate the performance of SCCN through extensive simulation studies. The results show that SCCN achieves satisfactory performance in increasing statistical power and spatial specificity while controlling the false-positive rate. Notably, SCCN is easily scalable to both small and large datasets. Besides, we apply SCCN to two real data examples: a nicotine-addiction research study, using UK Biobank[1] data with 3269 participants, and a schizophrenia research study with 330 participants. Through these applications we systematically investigate disease-related subnetwork structures using SCCN with rigorously controlled FWER.

[1]UK Biobank is a large-scale biomedical database and research resource containing in-depth genetic and health information from half a million U.K. participants.

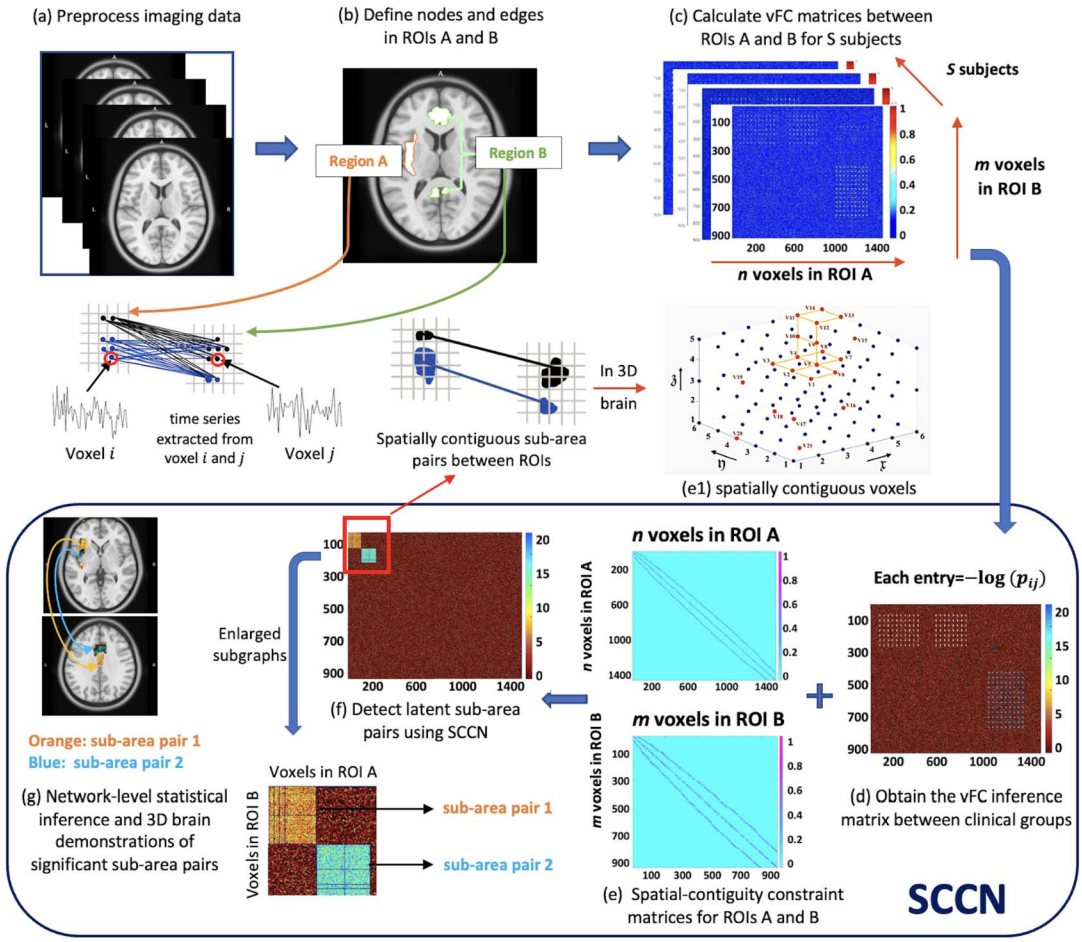

FIG. 2. *The vFC pattern extraction pipeline*: (*a*) *Preprocess the fMRI data and transform it into a standard brain template*. (*b*) *Define voxels in ROIs as nodes and bonds between voxels as edges. Extract the time series of brain signals from each voxel*. (*c*) *Calculate the connectivity matrix between voxels from regions A and B for each subject*. (*d*) *Calculate the connectivity inference matrix, where each element is a test statistic per edge between clinical groups. A brighter point in the heatmap suggests a larger between-group difference*. (*e*) *Construct the spatial-contiguity constraint matrices for ROIs A and B* (*see detailed matrix construction in Section* 2.1). *In* (*e*1), *each dot represents a voxel in* 3*D coordinates. Voxels connected by lines form a spatially contiguous area*. (*f*) *Detect the disease-related connections contained in subarea pairs based on* (*d*) *and* (*e*) *jointly.* (*f*) *is obtained by reordering the nodes in* (*d*), *with the densely altered subnetworks pushed to the top* (*i.e.*, (*d*) *and* (*f*) *are isomorphic graphs*). (*g*) *Conduct the proposed MDL-based network-level statistical inference. The subarea pairs that pass the statistical tests are highlighted.*

2. Methods.

2.1. *Background.*

2.1.1. *Data structure.* Given two ROIs, A and B, each consisting of n and m voxels, respectively, the vFC association patterns can be represented by a general $(n+m)\times(n+m)$ outcome matrix. Specifically, the $(n+m)\times(n+m)$ connectivity matrix can be decomposed into three submatrices: $n\times n$, $m\times m$, and $n\times m$, which encompass within-A, within-B, and between-region connections information. Herein, we focus on presenting the new methodology for vFC analysis between ROI A and B (i.e., $n\times m$ connectivity matrix), which is motivated by the growing interest in clinical investigations aimed at exploring neuropsychiatric disorder-related inter-regional vFC changes (Agosta et al. (2013), Rogers et al. (2007), Wu

et al. (2011)). Due to space limitation, we provide the statistical framework for within-region vFC analysis (i.e., the $n \times n$ and $m \times m$ connectivity matrices) along with the additional simulations and real data applications in Appendix B (Lu et al. (2024)).

For a subject $s \in [S] := \{1, \ldots, S\}$, let $\mathbf{Z}^{A,s}_{n\times T}$ and $\mathbf{Z}^{B,s}_{m\times T}$ represent the matrices of voxel-level blood-oxygenation-level dependent (BOLD) signals at T different time points for ROIs A and B. The outcome variables are the functional connectivity measures quantified by similarity matrices between the time series of voxels in A and in B. For example, Y^s_{ij}, the connectivity strength between voxel i in A and voxel j in B, can be computed by $Y^s_{ij} = f(Z^{A,s}_{i\cdot}, Z^{B,s}_{j\cdot})$, where $Z^{A,s}_{i\cdot}$ and $Z^{B,s}_{j\cdot}$ are the BOLD time series for voxels i and j and f is a similarity metric (e.g., Fisher's z-transformed Pearson correlation). Collecting all Y^s_{ij} for each voxel pair $(i, j) \in [n] \times [m]$ gives an interregion connectivity matrix $\mathbf{Y}^s_{n\times m}$. Additionally, a covariate vector $\mathbf{X}^s_{1\times p}$ is observed for each subject s, and this contains demographic and clinical information.

Our goal is to identify clinical/behavioral-related functional connectivity (FC) patterns at the voxel level. This is because voxel-level findings can reveal altered FC with improved statistical power and enhanced spatial specificity and resolution. To achieve this, multivariate statistical inference is required for the $n \times m$ vFC outcomes (usually in high dimension, e.g., millions) with spatial constraints. We first test the associations between each outcome Y^s_{ij} and a regressor of primary interest $x^s_1 \in \mathbf{X}^s$ (clinical status in our application, e.g., patient or control),

$$\mathbb{E}\big(Y^s_{ij}|\mathbf{X}^s\big) = \alpha_0 + x^s_1\beta_{ij} + \mathbf{X}^s_{1\times(p-1)}\boldsymbol{\alpha},$$

where β_{ij} is the coefficient of x^s_1 and $\boldsymbol{\alpha}$ is a coefficient vector for the remaining covariates $\mathbf{X}^s_{1\times(p-1)}$ (e.g., age, ethnicity, etc). We denote $\boldsymbol{\beta} := \{\beta_{ij}\}_{i\in[n],\, j\in[m]}$ and aim to systematically extract vFC whose $\boldsymbol{\beta} \neq 0$ with high accuracy. We further summarize the significance levels of $\boldsymbol{\beta}$ by a *connectivity inference matrix* $\mathbf{W}_{n\times m}$. Each entry of $\mathbf{W}_{n\times m}$ is computed by $\mathbf{W}_{ij} = -\log p_{ij}$, where p_{ij} is the p-value for β_{ij}. In neuroimaging statistics the selection of $\boldsymbol{\beta} \neq 0$ is not only determined by the level of statistical significance but also by spatial constraints. In addition to these two factors, $\boldsymbol{\beta}$ is also intrinsically linked with an underlying $n \times m$ bipartite graph between ROIs A and B. Therefore, we will require both graphic and spatial information to assist in identifying vFC whose $\boldsymbol{\beta} \neq 0$. We present the detailed graphic and spatial constructions as follows.

2.1.2. *Graph representation.* To decipher the complex voxel-pair connectome, we consider a bipartite graph structure $G = \{U, V\}$ underlying the inference matrix $\mathbf{W}_{n\times m}$. The node sets U and V represent voxels in ROIs A and B, respectively, where $|U| = n$ and $|V| = m$. We assume that, after spatial normalization and registration of the fMRI data, all subjects share a common set of nodes, namely, $(U^s, V^s) \equiv (U, V)$, $\forall s \in [S]$.

2.1.3. *Spatial contiguity.* Each node in our dataset corresponds to a voxel at a certain spatial position in 3D brain imaging (e.g., Figure 2(e1)). When we map each detected subgroup of voxels back to the 3D brain space, we desire these voxels to emerge as a spatially adjacent cluster (i.e., connected components). Such anticipation, translated into formal language, is referred to as *spatial contiguity*. Specifically, we define an "infrastructure graph" $\mathcal{S}_A$ between all nodes within ROI A to accommodate spatial contiguity. Each entry $S_{ii'}$ in $\mathcal{S}_A$ is a spatial-adjacency indicator variable between voxels i and i' in ROI A, where $S_{ii'} = 1$ if $d_{ii'} \leq \varepsilon$, and $S_{ii'} = 0$ otherwise ($d_{ii'}$ is the Euclidean distance between voxels i and i'). For example, in a 3D grid space, when ϵ is set to be $\sqrt{3}$, a centroid voxel i in a cube will have 26 surrounding voxels i' such that $S_{ii'} = 1$. We define and interpret $\mathcal{S}_B$ for nodes within ROI B

similarly. $\mathcal{S}_A$ and $\mathcal{S}_B$ will be used to prescribe the spatial-contiguity constraints when implementing SCCN. We provide more rigorous mathematical definitions of spatial contiguity, $\mathcal{S}_A$, and $\mathcal{S}_B$ in Appendix A.1 (Lu et al. (2024)).

We propose the SCCN model to systematically select vFC of $\beta_{ij} \neq 0$ by jointly considering the information of voxel-pair-level statistical significance, underlying graph structures, and spatial constraints. We integrate these into a weighted graph $\mathcal{G} = \{W, \mathcal{S}_A, \mathcal{S}_B\}$ as the input of our method.

2.2. *Detecting densely altered subarea pairs from an ROI pair.*

2.2.1. *Spatial-contiguity-constrained objective function.* The node set U, corresponding to voxels in ROI A, can reportedly be partitioned into mutually nonoverlapping subareas $\{U_c\}$, denoted by $U = \bigoplus_{c=1}^{C} U_c$ (Eickhoff et al. (2015)). Similarly, we have $V = \bigoplus_{d=1}^{D} V_d$ for ROI B. In this paper we aim to extract subarea pairs $\{(U_c, V_d)\}$ that dominantly contain disease-related voxel pairs, and we call these "densely altered" subarea pairs. Formally, a subarea pair (U_c, V_d) is considered densely altered if $\sum_{(i,j)\in(U_c,V_d)} \frac{I(\beta_{ij}\neq 0)}{|U_c|\,|V_d|} \gg \sum_{(i,j)\in(U_c',V_d')} \frac{I(\beta_{ij}\neq 0)}{|U_c'||V_d'|}$, where U_c' and V_d' are the complements of node sets U_c and V_d. We are, therefore, inspired to devise a regularized objective function to generate a checkerboard-like network structure underlying the connectivity inference matrix $\mathbf{W}$. This network structure reshuffles $\mathbf{W}$ and reveals densely altered $\{(U_c, V_d)\}$ pairs from (U, V). In addition, we impose spatial contiguity on U_c and V_d to improve biological interpretability and prohibit isolated false positive edges. Finally, the objective function is formulated as follows:

$$\underset{\substack{C,D,U=\bigoplus_{c=1}^{C} U_c, V=\bigoplus_{d=1}^{D} V_d \\ (U_c, V_d \text{ subject to spatial contiguity})}}{\operatorname{argmax}} \int \sum_{c=1}^{C}\sum_{d=1}^{D} \Bigg\{ \log \frac{\sum_{i\in U_c, j\in V_d} W_{ij} \cdot I(W_{ij} > r)}{|U_c||V_d|} + \lambda \log\big(|U_c||V_d|\big) \Bigg\} g(r)\, dr, \tag{1}$$

where $\lambda \in [0, 1]$ is a tuning parameter, r is a threshold below which there is no disease-related effect on W_{ij}, and $g(r)$ is the distribution function for r. Both $g(r)$ and λ can be chosen by prior knowledge or by a data-driven method proposed in Section 2.2.2.

The tuning parameter λ falls in the range $[0, 1]$: when $\lambda = 0$, maximizing (1) is equivalent to maximizing $f_1 = \frac{\sum_{i\in U_c, j\in V_d} W_{ij} \cdot I(W_{ij} > r)}{|U_c||V_d|}$, which is a popular definition for connection density; when $\lambda = 1$, maximizing (1) is simply maximizing $f_2 = \sum_{i\in U_c, j\in V_d} W_{ij} \cdot I(W_{ij} > r)$, which quantifies the magnitude of significant voxel pairs contained by the subarea pair (U_c, V_d). Direct optimization of the connection density f_1 tends to detect a dense subgraph with a minuscule size, while the optimization of f_2 can trigger an oversized subgraph. Theorem 1 shows that function (1) provides a consistent estimate for the targeted topological structure (collections of edge-induced subarea pairs) in the sense that the error of edge assignments is negligible in large region pairs. Extensive simulation studies also show that function (1) performs well in balancing the size and density when detecting subgraphs.

2.2.2. *Optimization of objective function* (1) *for given* $g(r)$ *and* λ. In this section we focus on optimizing function (1) for a given configuration of $g(r)$ and λ, which are the density function for the threshold r and the tuning parameter in (1). We will then discuss how to determine $g(r)$ and λ in the next section. Unfortunately, even with a given $g(r)$ and λ, direct optimization of (1) is still an NP-hard problem. Therefore, traditional optimization methods, such as gradient descent, cannot be used due to the nonconvexity of the problem. Here we

present an alternative strategy for optimizing (1). The essential idea is that we integrate $\mathbf{W}$ with the spatial-contiguity constraints and then estimate the targeted community structure using modified spectral clustering algorithms via iterative procedures. As presented earlier, the targeted network structure is $\{U_c, V_d\}$ partitioned from (U, V) (i.e., the collection of edge-induced subarea pairs, or in other words, the voxel memberships of U_c and V_d), where $U = \bigoplus_{c=1}^{C} U_c$ and $V = \bigoplus_{d=1}^{D} V_d$.

According to the spectral clustering algorithm, applying singular value decomposition to the Laplacian matrix of $\mathbf{W} = \mathbb{U}\mathbf{\Sigma}\mathbb{V}^\top$ and then clustering $\mathbb{U}$ and $\mathbb{V}$ will give partitions of regions A and B, respectively. Now, since $\mathbb{V}$ is the eigenvectors of $\mathbf{W}^\top\mathbf{W}$, spectral clustering on the Laplacian matrix of $\mathbf{W}^\top\mathbf{W}$ will simply give the partitions of Region B. Similarly, spectral clustering on the Laplacian matrix of $\mathbf{W}\mathbf{W}^\top$ will provide the partitions of Region A. Therefore, our community-detection algorithm can be conducted based on $\mathbf{W}\mathbf{W}^\top$ and $\mathbf{W}^\top\mathbf{W}$. Next, to incorporate the spatial-contiguity constraints into the optimization, we make use of the two within-region "infrastructure graphs" $\mathcal{S}_A$ and $\mathcal{S}_B$ introduced earlier. Specifically, we define

$$\mathbf{W_A} = \mathbf{W}\mathbf{W}^\top \odot \mathcal{S}_A \quad \text{and} \quad \mathbf{W_B} = \mathbf{W}^\top\mathbf{W} \odot \mathcal{S}_B, \tag{2}$$

where $\odot$ is an elementwise product. As pointed out by Kamvar, Klein and Manning (2003) and Craddock et al. (2012), $\mathcal{S}_A$ and $\mathcal{S}_B$ force the similarity between all pairs of nonadjacent voxels to zero, which breaks edges between isolated voxels in the graph. Based on this, the n by n matrix $\mathbf{W}_A(ii')$ (where i and i' are two voxels in A) is greater if the voxels in A are spatially adjacent and have a similar profile linking to voxels in Region B. The spatial-contiguity constraints enable our method to produce results that better honor the neurobiological background regarding the coherence of neighboring neuron populations (Thirion et al. (2006)).

We can now fit a stochastic block model to $\mathbf{W}_A$ (and another to $\mathbf{W}_B$), using the spectral clustering algorithm, and then grid search for the optimizer of function (1). We further examine whether the estimated $\widehat{U}_c$ and $\widehat{V}_d$ values satisfy the spatial-contiguity constraints, while empirically we find that the constraints are typically satisfied. There is thus no need to perform any further modification step for the constraints. We formally present our clustering procedure in Algorithm 1.

Consistency for subgraph detection. In Lemma 1 we first establish that, given true subareas numbers C^* and D^*, the solution to optimize the objective function (1) provides a consistent estimate for the topological structure of the target community ($\{U_c, V_d\}$) (the collection of edge-induced subarea pairs) in the sense that false-positive edge assignments are negligible

Algorithm 1 Optimization of objective function (1) with given λ

procedure ALGORITHM (Input: λ and $\mathcal{G} = \{\mathbf{W}, \mathcal{S}_A, \mathcal{S}_B\}$)
  function *SCCN.partition* (λ, $\mathcal{G}$)
  for $C = 1, 2, \ldots, |U|$ **do**
    Ratio-cut spectral clustering $\mathbf{W}_A$ into C networks: $U = \bigoplus_{c=1}^{C} U_c$
    for $D = 1, 2, \ldots, |V|$ **do**
      Ratio-cut spectral clustering $\mathbf{W}_B$ into D networks: $V = \bigoplus_{d=1}^{D} V_d$
      Substitute network sets U and V into objective function (1), and obtain the output values
    end for
  end for
  return C, D, $U = \bigoplus_{c=1}^{C} U_c$ and $V = \bigoplus_{d=1}^{D} V_d$ that yield the maximum output value
  end function
end procedure

in very large bipartite graphs $G = (U, V)$, $|U| \to \infty$, and $|V| \to \infty$. Then we establish the convergence of Algorithm 1 to optimize function (1) based on Theorems 1 and 2. In Theorem 1 we prove that our algorithm can provide a consistent estimate of the number of subareas, C and D. In Theorem 2 we prove that the implementation of Algorithm 1 converges to the optimal solution of the objective function (1).

To present the theoretical results, we consider the following settings. Let $\{e_{ij}^1\}$ and $\{e_{ij}^0\}$ be the sets of positive (e.g., disease-related) and negative edges, respectively. For a weighted matrix $\mathbf{W}$, we assume that $w_{ij}|e_{ij}^1 \overset{\text{iid}}{\sim} f_1$ and $w_{ij}|e_{ij}^0 \overset{\text{iid}}{\sim} f_0$, where f_1 and f_0 are two probability density functions with means and variances (μ_1, σ_1^2) and (μ_0, σ_0^2), respectively. In addition, let $\mathcal{M}^*$ be the true membership of edges (the community index of edges falling in subarea pair (U_c, V_d)). Furthermore, let $\widehat{\mathcal{M}}_{(\widehat{C},\widehat{D})}$ be the membership estimated by function (1) with $\widehat{C}$ subareas in Region A and $\widehat{D}$ subareas in Region B.

LEMMA 1 (Consistency with known subarea numbers C^* and D^*). *Assume that* $\mathbb{E}(\mathbf{W}\mathbf{W}^{\mathbf{T}})$ *is of rank* C^* *with smallest absolute nonzero eigenvalue of at least* Λ_A, *and* $\mathbb{E}(\mathbf{W}^{\mathbf{T}}\mathbf{W})$ *is of rank* D^* *with smallest absolute nonzero eigenvalue of at least* Λ_B. *Assume further that* $\max(\mu_0, \mu_1, \sigma_0^2, \sigma_1^2) \le d$ *for some* $d \le \max(\log n/n, \log m/m)$). *Then if there exists* $(2+\varepsilon_A)\frac{ndCD}{\Lambda_A^2} < \tau_A$ *and* $(2+\varepsilon_B)\frac{mdCD}{\Lambda_B^2} < \tau_B$ *for some* $\tau_A, \tau_B, \varepsilon_A, \varepsilon_B > 0$, *the output* $\widehat{\mathcal{M}}_{(\widehat{C},\widehat{D})}$ *that maximizes function* (1) *is consistent to the true membership* $\mathcal{M}^*_{(C^*,D^*)}$ *underlying the latent community structure up to a permutation.*

Equivalently, let $\widehat{S}_c$, $\widehat{S}_d$ *be the estimated node sets for the subgraphs* G_c, G_d (*induced by* U_c *and* V_d), *respectively. Then* $\widehat{S}_c \cap U_c$ *represents the nodes in* G_c *whose assignments can be guaranteed.* $\widehat{S}_d \cap V_d$ *follows the same definition. With probability at least* $1 - \max(n, m)^{-1}$, *up to a permutation, we have*

$$\sum_{c=1}^{C}\sum_{d=1}^{D}\left[1 - \frac{|(\widehat{S}_c \cap U_c) \otimes (\widehat{S}_d \cap V_d)|}{|U_c||V_d|}\right] \le \tau_A^{-1}(2+\varepsilon_A)\frac{ndCD}{\Lambda_A^2} + \tau_B^{-1}(2+\varepsilon_B)\frac{mdCD}{\Lambda_B^2},$$

where $\otimes$ *denotes the edge set that connects two node sets on its left and right sides.*

THEOREM 1 (Consistency for grid-searched C, D). *Let the sizes of subgraph pairs* $|U_c| \times |V_d| (\forall c = [C^*], d = [D^*])$ *be generated from a multinomial distribution with probabilities* $\boldsymbol{\pi} = (\pi_1, \ldots, \pi_{C^* \times D^*})$. *Assume* $\exists \delta > 0$ *such that*

$$\mu_1 > \mu_0 \frac{1+\delta}{1-\delta}\left(1 + \sqrt{1 + \frac{\pi_{\min}^2}{\pi_1^2 + \cdots + \pi_{C^* \times D^*}^2}}\right),$$

then under conditions in Lemma 1 and tuning parameter $\lambda = 0.5$, *the number of misassigned edges* N_{edge} *satisfies*

$$N_{\text{edge}} = o_p(n_{\min} * m_{\min}) \quad \text{as } |U|, |V| \to \infty,$$

where $n_{\min}$, $m_{\min}$ *are the sizes of the smallest possible subgraphs in* U *and* V, *respectively.*

THEOREM 2 (Convergence of Algorithm 1). *Let* $\tilde{U} = \bigoplus_{c=1}^{\tilde{C}} U_c$, $\tilde{V} = \bigoplus_{d=1}^{\tilde{D}} V_d$ *be the partitions yielded by ratio-cut spectral clustering on* $\mathbf{W}_A$ *and* $\mathbf{W}_B$ *that maximizes function* (1) *with cluster numbers* $\tilde{C}$, $\tilde{D}$. *Then* $\tilde{U}$, $\tilde{V}$ *converge almost surely to the true community structure where false-positive edge assignments to each subbicluster are negligible.*

PROOF. Proofs of Lemma 1 and Theorems 1 and 2 are provided in Appendix C (Lu et al. (2024)). □

In summary, the above results provide theoretical evidence that the solution of the proposed objective function (1) and Algorithm 1 converge to the target community structure ($\{U_c, V_d\}$). Moreover, extensive simulation analyses in multiple settings with a wide range of different sample sizes demonstrate that SCCN can accurately reveal the true community structure with low false-positive and false-negative rates.

2.2.3. *Determining $g(r)$ and λ.*

(i) *Determining $g(r)$.* Following Efron (2010), we can choose $g(\cdot)$ to be a discrete distribution on thresholds $\{r_1, \ldots, r_p\}$. A simple example would be as follows. Suppose that the voxel-pair-level FDRs yielded by preselected thresholds r_1, r_2, and r_3 are 0.20, 0.10, and 0.05, respectively. We can then assign a higher probability mass to r_p that yields a lower FDR, for example, $g(r_1) = 0.1$, $g(r_2) = 0.3$, and $g(r_3) = 0.6$. In addition, r_1, r_2, and r_3 can be chosen from commonly used thresholds in MRI studies, such as $-\log(0.005)$ and $-\log(0.001)$ (W_{ij} is $-\log p_{ij}$ after screening, and r is a threshold for W_{ij}).

(ii) *Selecting λ.* As aforementioned, the tuning parameter λ adjusts the balance between the subgraph size and the connection density; it thus plays a critical role in our method. A large λ encourages large $|U_c|$ and $|V_d|$, whereas a small λ is stricter on the connection densities of (U_c, V_d) pairs. Essentially, the selection of λ is related to the network structure of β_{ij}. In practice, we have observed from many datasets that the coefficients $\beta_{ij} \neq 0$ usually exhibit a block model. To reflect this, we assume the following hierarchical model. Suppose there exists a nonrandom, latent hyperparameter $\boldsymbol{\beta} \in \mathbb{R}^{n \times m}$ with all nonzero elements. We can generate a bipartite similarity matrix $\eta \in \{0, 1\}^{n \times m}$ from a bipartite stochastic block model with blocks $\{(U_c, V_d)\}$ and the corresponding connection probabilities $\{\pi_{ij}\}$ such that $\eta_{ij} \sim$ Bernoulli(π_{ij}) are independent of each other, where

$$\pi_{ij} = \begin{cases} \pi_{cd}(\lambda) & i \in U_c, j \in V_d, \\ \pi_0(\lambda) & \text{otherwise.} \end{cases}$$

We select the λ value that maximizes the likelihood for this block model. In practice, the η_{ij} values are not directly observable, and we replace them by $\eta_{ij}(r_0) := I(w_{ij} > r_0)$. The log-likelihood function for λ is

$$\begin{aligned} &l_\lambda\big(\pi_{cd}, \forall c \in [C], d \in [D] | \eta_{ij}(r_0)\big) \\ &\quad = \sum_{c,d} \sum_{(i,j) \in U_c \times V_d} \eta_{ij}(r_0) \log \pi_{cd} + \big(1 - \eta_{ij}(r_0)\big) \log(1 - \pi_{cd}). \end{aligned}$$

To eliminate the arbitrariness in choosing the threshold r_0, we integrate the likelihood function with respect to r_0 over a prior distribution $g_0(r_0)$ determined by the method above. This yields the following criterion:

$$\lambda_{\text{optimal}} = \operatorname*{argmax}_\lambda \left\{ \int \max_{U_c, V_d, \pi_{cd}} l_\lambda^r\big(\pi_{cd}(\lambda), \forall c = [C], d = [D] | \eta_{ij}(r_0)\big) g_0(r_0)\, dr_0 \right\}.$$

We formally present the procedure to select the tuning parameter λ in Algorithm 2. The overall complexity of the algorithm is $O(Knm)$, where K is a sufficient searching range for λ, $n = |U|$, and $m = |V|$.

Since the inference results between clinical groups across S subjects are captured in $\mathbf{W}$, the algorithm complexity no longer involves sample size S, indicating the scalability of SCCN for large datasets. In addition, clustering algorithms typically involve computing the first K

Algorithm 2 Grid search for λ

procedure ALGORITHM
  for $0 \le \lambda \le 1$ **do**
    return $U = \bigoplus_{c=1}^{C} U_c$ and $V = \bigoplus_{d=1}^{D} V_d$ from *SCCN.partition* function in Algorithm 1
    for $r_0 = (r_0)_1$ to $(r_0)_q$ **do**
      Compute the log-likelihood: $l_\lambda(\widehat{\pi}_{c\times d}^{\mathrm{MLE}}, \forall c = [C], d = [D] | \eta_{ij}(r_0))$
    end for
    Integrate the log-likelihood w.r.t. r_0:
    $l_\lambda = \sum_{i=1}^{p} L_\lambda(\widehat{\pi}_{c\times d}^{\mathrm{MLE}}, \forall c = [C], d = [D] | \eta_{ij}(r)) g((r_0)_i)$
  end for
  return $\widehat{\lambda}$ that yields maximized l_λ
end procedure

eigenvectors of a potentially high-throughput similarity matrix. Our input similarity matrix $\mathbf{W}$ is sparse after applying screening and the spatial-contiguity constraints (usually only 0.2%–5.0% of edges are nonzero entries after processing), which notably reduces computational expense. It is, however, worth noting that since our algorithm is based on a single region pair, the computational burden may become heavy when investigating multiple different pairs, especially when a whole-brain analysis is needed.

2.3. *Statistical inference of* $\{(U_c, V_d)\}$ *pairs*. Recall that our ultimate goal is to extract a few most-densely connected subgraph pairs from $\{(U_c, V_d)\}$ based on the block partition $\{U_c, V_d : c \in [C], d \in [D]\}$ that we have already obtained at this point. A natural idea is to inspect each (U_c, V_d) pair and perform a statistical test on them with the alternative hypothesis that the subgraph $U_c \otimes V_d$ is unusually dense. Here we devise a clusterwise permutation test (Nichols and Holmes (2002)) with FWER control. The hypotheses are

$$\mathbb{H}_0 : \text{Subgraph } U_c \otimes V_d \text{ is not unusually dense},$$

$$\mathbb{H}_a : \text{Subgraph } U_c \otimes V_d \text{ is unusually dense}.$$

More specifically, under $\mathbb{H}_0$, the connection density of $U_c \otimes V_d$ should be close to the density of subarea pairs obtained by randomly shuffling edges in the bipartite graph. Built upon the minimum description length (MDL) principle proposed by Grünwald (2007), we derive the following MDL-based test statistic:

$$\mathrm{MDL}(U_c, V_d) = \log_2\left[\binom{n}{|U_c|}\binom{m}{|V_d|}\right] + \left(\frac{1-\mu_1^2}{2\ln 2} - L_\zeta\right)|U_c| \times |V_d|,$$

where μ_1 is the mean value of edgewise test statistics ζ_{ij} for edges within $U_c \times V_d$, and $L_\zeta = -\int \phi(\zeta_{ij}) \log_2(\phi(\zeta_{ij}))\, d\zeta_{ij} + C$ is an information entropy measure based on the standard normal distribution ϕ for ζ_{ij}. Detailed derivations for the MDL-based test statistic and its connections to our inference goal are provided in Appendix C.4 (Lu et al. (2024)). We formally present the clusterwise permutation test for each observed subarea pair (U_c, V_d) in Algorithm 3. The number of permutations H in this algorithm can be determined based on the sample size, the targeted computational expense, and the precision of the test. For example, $H = 1000$. Compared to conventional multiple testing correction methods (e.g., FDR and FWER), the MDL-based clusterwise permutation test returns suppressed false-positive findings and shows improved statistical power in real-data examples and simulations.

Algorithm 3 MDL-based clusterwise permutation test for each (U_c, V_d) pair

procedure ALGORITHM
  Compute $T^0_{c,d} = \text{MDL}(U_c, V_d)$ for each (U_c, V_d) pair yielded with true covariate labels
  for $h = 1, \ldots, H$ **do**
    Permute covariate labels and obtain the new inference connectivity matrix $\mathbf{W^h}$
    Obtain $U^h = \bigoplus_{c=1}^{C} U_c^h$ and $V^h = \bigoplus_{d=1}^{D} V_d^h$ by substituting $\mathbf{W^h}$ in Algorithms 1 and 2
    return $T^h = \max(\text{MDL}(\text{U}_\text{c}^\text{h}, \text{V}_\text{d}^\text{h}))$
  end for
  Compute p-value for each observed (U_c, V_d) pair: $P_{c,d} = \frac{\sum I(T^h > T^0_{c,d})}{H}$
  return the significance of each observed (U_c, V_d) pair based on $P_{c,d}$ at a predetermined α-level
end procedure

3. Experiments. In this section we apply SCCN to two real datasets to investigate the voxel-level altered connections under different clinical settings. Dataset 1 contains 3269 participants from a nicotine-addiction study using fMRI data collected from the UK Biobank database. Dataset 2 includes 330 participants from a schizophrenia (SZ) research study using fMRI data collected in Baltimore, MD.

3.1. *Nicotine-addiction research study.*

Sample characteristic. Our primary dataset consists of 3269 individuals from the UK Biobank database, including 1353 current smokers (M/F: 737/616, age: 48.6 ± 15.3) and 1916 previous light smokers (M/F: 1187/729, age: 32.9 ± 18.1). Detailed information on the selection of these 3269 subjects is provided in Appendix E.1 (Lu et al. (2024)). Specifically, we define *current smokers* as participants who currently smoke more than 10 cigarettes per day, indicating nicotine addiction.[2] Conversely, we define *previous light smokers* as individuals who had tried only a few cigarettes in the past but are not currently addicted to nicotine products, serving as controls.[3] For detailed information on fMRI imaging acquisition and preprocessing procedures, please refer to Appendix E.2 (Lu et al. (2024)).

Clinical background. Abundant literature shows that the basal ganglia (BG), hippocampus (Hippo), and insular gyrus (Ins) play important roles in nicotine addiction (Ersche et al. (2011), McClernon et al. (2016), Gaznick et al. (2014)). We, therefore, intend to look into the disrupted connectivity patterns between these three bilateral ROIs, resulting in a total of 12 pairs. To maintain conciseness, we present the results for the (left BG, left Ins) pair in the main text, while the remaining 11 cases are provided in Appendix E.4 (Lu et al. (2024)). By investigating the altered vFC patterns across different clinical groups, we aim to gain insights into the underlying neurological mechanisms of nicotine dependence and ultimately assist smokers in resisting nicotine cravings.

We labeled the left BG and left Ins using the Brainnetome Atlas (Fan et al. (2016)) (left BG: 2345 voxels; left Ins: 1762 voxels). For each subject we calculated the vFC matrix between the left BG and left Ins, with each entry representing a Fisher's z-transformed Pearson correlation coefficient. Next, we calculated the population-level statistical inference ma-

[2]ACE touchscreen question, "About how many cigarettes do you smoke on average each day?".
[3]ACE touchscreen question, "In the past, how often have you smoked tobacco?".

trix across all subjects while adjusting for: (i) demographic variables: age, sex, site, educational level, and body mass index (BMI); (ii) imaging confounds: head motion (quantified through the mean displacement (in mm) between consecutive time points in rs-fMRI) and four confounding factors pertain to the position of the head and the radio-frequency receiver coil in the scanner. More details regarding the selection and description of these covariates can be found in Appendix E.3 (Lu et al. (2024)). Following this, we applied SCCN and the MDL-based test to identify anomalous subarea pairs from $\mathbf{W}^{(\mathrm{BG}_{\mathrm{left}},\mathrm{Ins}_{\mathrm{left}})}$, taking into account spatial-contiguity constraints. Lastly, we juxtaposed these findings against outcomes obtained through comparative methods.

Network-level results. Each entry in the inference matrix $\mathbf{W}^{(\mathrm{BG}_{\mathrm{left}},\mathrm{Ins}_{\mathrm{left}})}$ is endowed with a $-\log p$ value testing the vFC difference between current smokers and previous light smokers (Figure 3(1)). Implementing Algorithm 2 returned the MLE $\widehat{\lambda} = 0.75$. Given the estimated $\widehat{\lambda}$, Algorithm 1 returned the number of clusters $\widehat{C} = 307$, $\widehat{D} = 212$ for $\mathbf{W}^{(\mathrm{BG}_{\mathrm{left}},\mathrm{Ins}_{\mathrm{left}})}$. The MDL-based test returned six abnormal subarea pairs, which are marked in red in Figure 3(2). A 3D demonstration of the detected subarea pairs from $\mathbf{W}^{(\mathrm{BG}_{\mathrm{left}},\mathrm{Ins}_{\mathrm{left}})}$ is shown in Figure 3(a)–(e) (with a significance level of 0.05 selected for the MDL-based permutation test). All extracted subarea pairs show well-organized topological structures. Results indicate that the majority of aberrant vFC patterns from $\mathbf{W}^{(\mathrm{BG}_{\mathrm{left}},\mathrm{Ins}_{\mathrm{left}})}$ are gathered between the medial inferior part of the left basal ganglia and the left insula.

Biological interpretation of detected subareas. The detected subareas consist of several locations that are believed to be frequently associated with nicotine addiction, including the medial inferior part of the basal ganglia and the posterior insula. We also observed decreased connectivity within these regions in current smokers, which aligns with the previous medical discovery that decreased resting-state functional connectivity is correlated with increased nicotine-addiction severity (Fedota and Stein (2015), Sutherland and Stein (2018)). The incorporated spatial-contiguity constraints help unfold the subareas within the BG, Hippo, and Ins, which maximally cover addiction-related vFC. These novel findings improve the spatial specificity of addiction-related locations in the three brain regions and may lead to future guidance for resisting the urge to use nicotine products.

Comparisons with existing methods. For comparison purposes, we again performed the BH-FDR correction edgewisely and BSGP clusterwisely on $\mathbf{W}^{(\mathrm{BG}_{\mathrm{left}},\mathrm{Ins}_{\mathrm{left}})}$. By first conducting an initial edgewise significance test across the current and previously light smoker groups, only 7.31% of the edges were found to be significant ($p < 0.005$). However, no edges showed significance after applying BH-FDR correction with $q = 0.01$ (Figure 3(3)). When applying BSGP to $\mathbf{W}^{(\mathrm{BG}_{\mathrm{left}},\mathrm{Ins}_{\mathrm{left}})}$, only one abnormal subarea pair was detected (Figure 3(4)), with 49.7% edges of $p > 0.005$ included in the detected pair, compared to 3.12% yielded by SCCN. In comparison to the two existing methods, SCCN yields much more densely altered vFC contained in spatially contiguous subarea pairs with strong topological structures.

3.2. *Schizophrenia research study.*

Sample characteristics. Our primary dataset contains 330 individuals, including 148 SZ patients (M/F 84/64, age 37.5 ± 14.4) and 182 healthy controls (M/F 80/102, age 37.0 ± 16.1). The participants were required for a large ongoing study of the effects of cognitive deficits in SZ. Specifically, the study probed how cognitive deficits contributed to functional disability in SZ patients and how they were related to altered functional networks that serve cognition. All subjects were assessed at local research centers in the greater Baltimore area

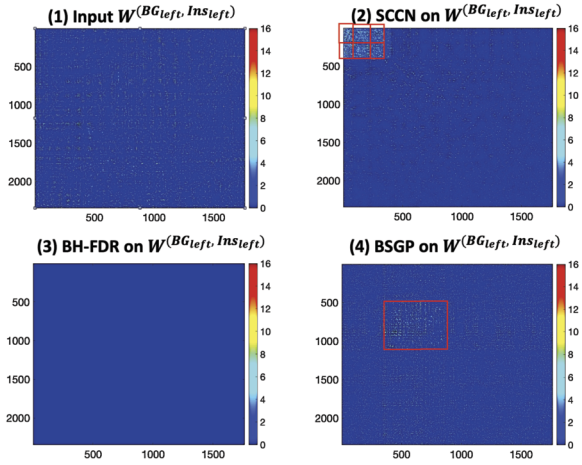

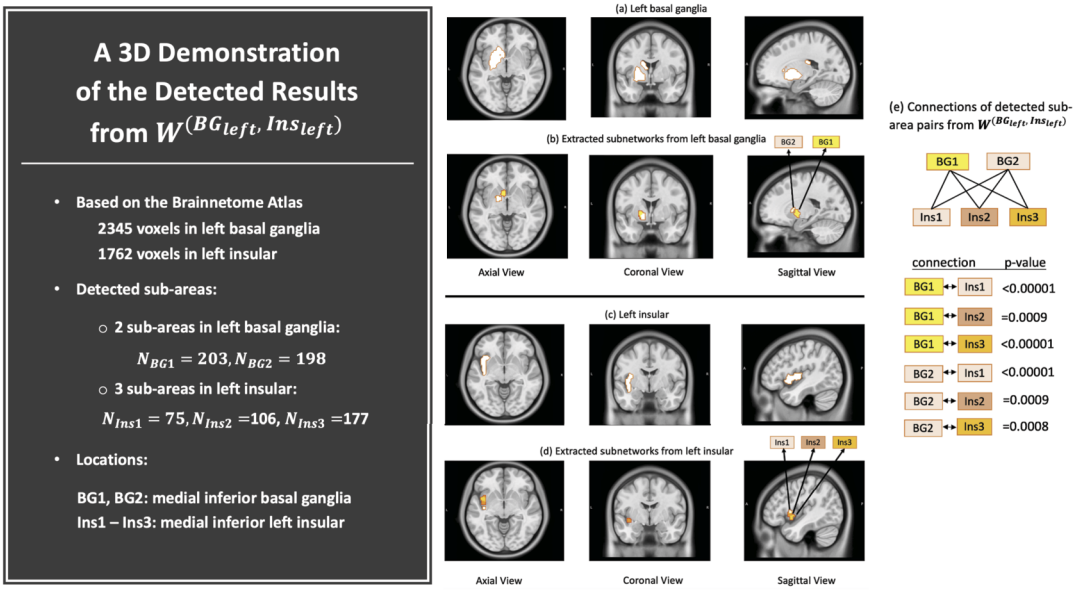

FIG. 3. *Detected subarea pairs from a nicotine-addition study*: (1) *A heatmap of* $\mathbf{W}^{(\mathrm{BG_{left}}, \mathrm{Ins_{left}})}$: *Rows and columns correspond to voxels from the left basal ganglia and the left insular, respectively.* (2) *Results yielded by SCCN*: *Altered subarea pairs that pass the MDL-based permutation test are highlighted in bold boxes.* (3) *Results yielded by BH-FDR*: *The hypothesis testing error measure was set to be* $q = 0.05$ *as a cut-off. No subarea pairs were detected.* (4) *Results yielded by BSGP*: *Only one positive yet much less dense subarea pair was detected. The detected subarea pair also lack spatial contiguity and specificity.* (*a*)–(*d*) *shows the 3D demonstration of the six detected altered subareas from* $\mathbf{W}^{(\mathrm{BG_{left}}, \mathrm{Ins_{left}})}$. (*a*)–(*e*) *show a 3D demonstration of the detected results from* $\mathbf{W}^{(\mathrm{BG_{left}}, \mathrm{Ins_{left}})}$. *Based on the p-values from the MDL-based permutation test shown in* (*e*), *most positive subarea pairs are located in the medial inferior part of the left basal ganglia and left insular.*

between 2004 and 2016 using uniform recruitment criteria as well as neurological and clinical assessments. Detailed information about participant demographics, the recruitment process, imaging acquisition, and fMRI preprocessing procedures can be found in Appendix D.1 (Lu et al. (2024)).

3.2.1. *Salience network disrupted connectivity.*

Clinical background. The salience network, which is mainly composed of the bilateral insula and cingulate cortices, is related to several core SZ symptoms. A vast amount of literature in neuroimaging research suggests that the connectivity in the salience network is disturbed during information processing in SZ patients (Palaniyappan, White and Liddle (2012)). We, therefore, intend to focus on the bilateral insula and cingulate cortices and study the schizophrenic-altered vFC patterns between them. Specifically, we want to extract schizophrenic-impacted edges that connect voxels from spatially coherent subareas within the insula to those within the cingulate cortex. This data-driven extraction of subareas caused by vFC abnormality in SZ may provide insights for more effective clinical treatments (e.g., by transcranial magnetic stimulation or deep-brain-stimulation therapies). We labeled the bilateral insula and cingulate cortices based on the Brainnetome Atlas (Fan et al. (2016)) (left insula: 1762 voxels; right insula: 1577 voxels; cingulate cortex: 5768 voxels). We applied SCCN and the MDL-based test to the edgewise connectivity inference matrices $\mathbf{W}^L_{1762\times5768}$ and $\mathbf{W}^R_{1577\times5768}$ for the (left Ins, cingulate) and (right Ins, cingulate) ROI pairs, respectively, while adjusting for age, sex, head motion (quantified through the mean displacement (in mm) between consecutive time points in rs-fMRI), and four imaging variables describing various aspects of the positioning (scanner lateral, transverse, and longitudinal brain position and scanner table position). $\mathbf{W}^L$ and $\mathbf{W}^R$ were obtained by the same computational procedures as in Dataset 1. Lastly, we compared the detection results with those obtained by comparative methods.

Network-level results. Each element in the vFC inference matrix $\mathbf{W}^L$ is $\mathbf{W}^L_{ij} = -\log(p^L_{ij})$, where p^L_{ij} is the p-value testing the case-control vFC difference for the (i, j) pair between the left insula and cingulate cortex (Figure 4(L1)). We then perform screening on $\mathbf{W}^L$ using a preselected threshold (e.g., $p = 0.05$): $\mathbf{W}^L_{ij} = (\mathbf{W}^L)_{ij} \cdot I((\mathbf{W}^L)_{ij} \le -\log(0.05))$. The postscreened inference matrix $\mathbf{W}^L$ can effectively exclude most noninformative false-positive edges while maintaining a high proportion of true-positive edges (Fan and Lv (2008), Li, Zhong and Zhu (2012)). Similar settings apply to $\mathbf{W}^R$ (Figure 4(R1)). Implementing Algorithm 2 returned a maximum-likelihood estimation (MLE) of $\widehat{\lambda}_L = 0.625$ for $\mathbf{W}^L$ and $\widehat{\lambda}_R = 0.85$ for $\mathbf{W}^R$. Given the estimated $\widehat{\lambda}$, Algorithm 1 returned the number of clusters $\widehat{C}_L = 135$ in the left insular, $\widehat{D}_L = 103$ in the cingulate for $\mathbf{W}^L$. For $\mathbf{W}^R$, $\widehat{C}_R = 223$ in the left insular, and $\widehat{D}_R = 220$ in the cingulate. The MDL-based test returned nine abnormal subarea pairs for $\mathbf{W}^L$ and 10 abnormal subarea pairs for $\mathbf{W}^R$ (marked in red in Figure 4(L2) and (R2)). A 3D demonstration of the detected results from $\mathbf{W}^L$ is shown in Figure 5 (using a significance level of 0.05 from the MDL-based permutation test). Information regarding the precise sizes, p-values, and locations is also specified in Figure 5. All extracted subarea pairs show well-organized topological structures. Overall, the aberrant vFC patterns from $\mathbf{W}^L$ are gathered between the dorsal insula and anterior cingulate cortex (ACC). Detailed detection results for $\mathbf{W}^R$ are provided in Appendix D.2 (Lu et al. (2024)).

Biological interpretation of detected subareas. The detected subareas consist of several well-known brain regions that are believed to be frequently associated with SZ disorder, including, most remarkably, the anterior insula (AI) and ACC. Emotions that most strongly engage the AI, such as anger and fear, are those that SZ patients tend to have the most difficulty recognizing (Wylie and Tregellas (2010)). Furthermore, the densities of neurons, axons, and synapses are found to be abnormal in the ACCs of people with SZ (Arnold and Trojanowski (1996)). All of the aberrant edges detected showed decreased or equivalent connections in SZ patients. This aligns with medical findings that SZ is a "dysconnectivity" disorder with primarily reduced FC across the salience network (Lynall et al. (2010)), although medication

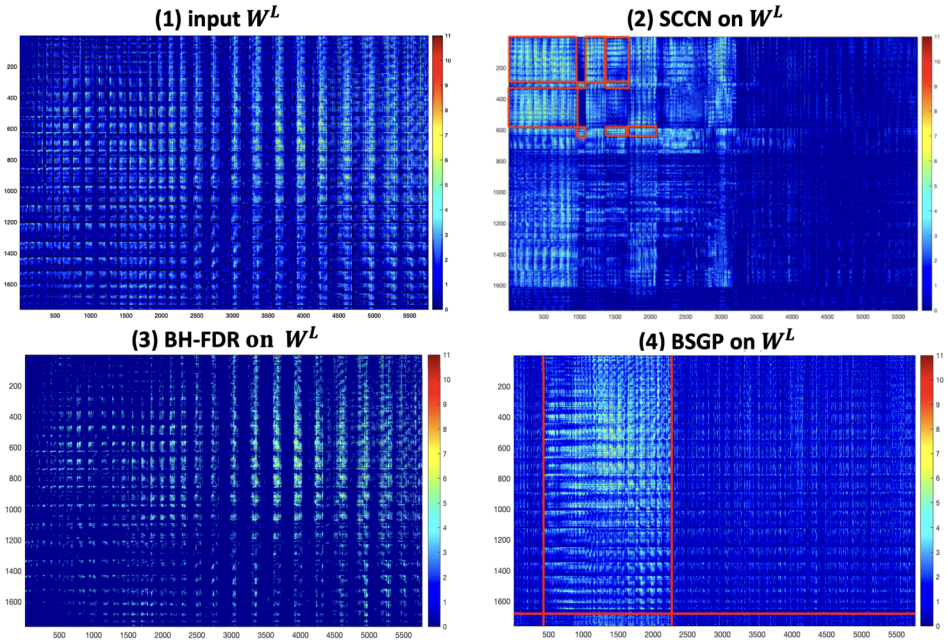

FIG. 4. *Detected subarea pairs in salience network from a schizophrenia study* (2*D*): (1) *A heatmap of* $\mathbf{W}^L$: *rows and columns correspond to the voxels from the left insula and the cingulate cortex, respectively. A brighter entry indicates a more differentially expressed voxel pair between clinical groups adjusted for other covariates.* (2) *Results yielded by SCCN: positive subarea pairs that pass the MDL-based permutation test are highlighted in bold boxes. There are many edges with small p-values outside the bold boxes* (*e.g., in the bottom left corner*) *because they are not spatially contiguous to those inside the boxes and are automatically excluded by SCCN.* (3) *Results yielded by BH-FDR: with* $q = 0.05$, *no subarea pairs were detected.* (4) *Results yielded by BSGP: only one informative yet much less dense subarea pair was detected. The detected subarea pair was also lack of spatial contiguity and specificity.*

effects cannot be completely ruled out. The imposed spatial-contiguity constraints help unfold brain subareas of the bilateral insula and cingulate cortices that maximally cover disease-related vFC. These novel findings improve the spatial specificity of SZ-related dysconnectivity in the well-known salience network and may lead to guidance for future treatments.

Comparisons with existing methods. For comparison purposes, we performed the Benjamini–Hochberg FDR (BH-FDR) correction edgewisely and a commonly used biclustering algorithm, bipartite spectral graph partitioning (BSGP), clusterwisely. By first conducting an initial correlation analysis between vFC and schizophrenic status, 17.83% of the edges in $\mathbf{W}^L$ were found to have $p < 0.005$ significance, where $p = 0.005$ is a commonly used yet uncorrected threshold in neuroimaging studies (Derado, Bowman and Kilts (2010)). After applying BH-FDR correction, 9.45% of the edges were found to be significant using the threshold of $q = 0.01$ (Figure 4(L3)), and no community structure was revealed. For $\mathbf{W}^R$ 13.51% of edges had p-values less than 0.005, and only 3.60% significant edges were found after BH-FDR correction with $q = 0.01$ (Figure 4(R3)); again, no community structure was found in $\mathbf{W}^R$. When applying BSGP to both $\mathbf{W}^L$ and $\mathbf{W}^R$, only one abnormal subarea pair was detected (Figure 4(L4) and (R4)), with more than 36.80% edges of $p > 0.005$ included compared to SCCN. In comparison to the existing methods, SCCN yields much more densely schizophrenia-associated vFC contained in spatially contiguous subarea pairs with stronger topological structures.

3.2.2. *Temporal-thalamic disrupted connectivity.* In contrast to the reduced salience network connections in SZ patients, many studies have shown that SZ patients have greater

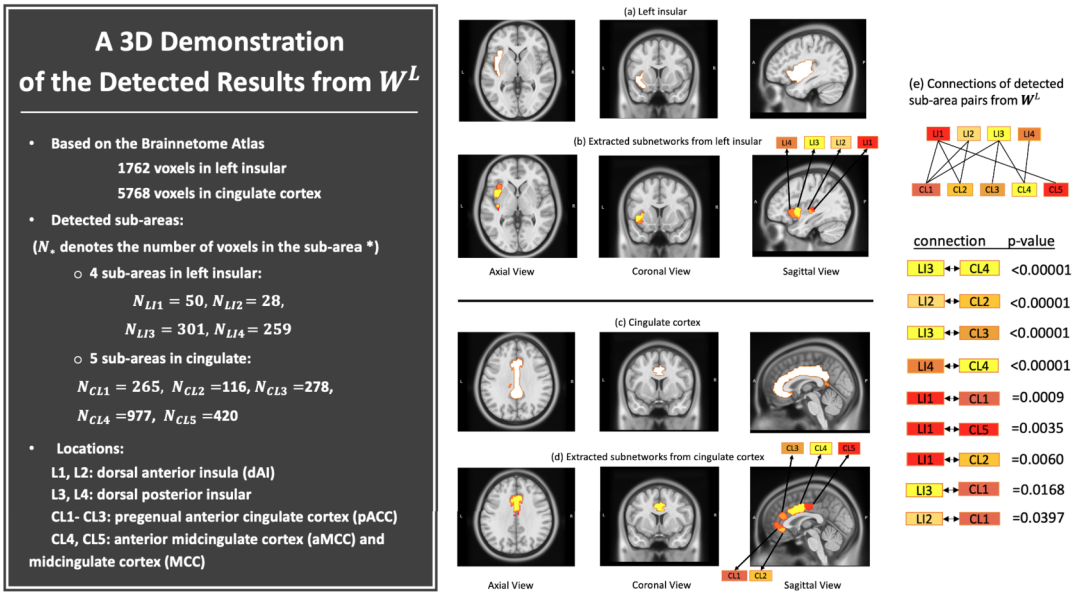

FIG. 5. *Detected subarea pairs in salience network from a schizophrenia study* (3D). *Let* LI_i *be the* i*th dysconnected subarea detected from the left insula that is connected to the* j*th subarea from the cingulate cortex,* CL_j. *Let* N_{LI_i} *denote the number of voxels in subarea* LI_i *and, similarly,* N_{CL_j} *for* CL_j. (*a*) (*c*) *show the images of the original left insular and cingulate cortex*; (*b*) *shows the SZ-affected subareas in the left insular that are connected to those in the cingulate cortex highlighted in* (*d*); (*e*) *shows the architecture of interconnections between the detected subareas from* $\mathbf{W}^L$ *and the associated* p*-values from the MDL-based permutation test. A* 3*D demonstration of the detected results from* $\mathbf{W}^R$ *is provided in Appendix D.*2 (*Lu et al.* (2024)).

thalamic connectivity with multiple sensory-motor regions, including, most remarkably, the temporal gyrus (Ferri et al. (2018), Çetin et al. (2014)). More specifically, thalamus to middle temporal gyrus connectivity was positively correlated with many core SZ features, such as hallucinations and delusions. We, therefore, aim to use SCCN to identify some novel findings between the middle temporal gyrus on the right hemisphere and the bilateral thalamus in SZ patients. Based on the Brainnetome Atlas, there are 3566 voxels in the right middle temporal gyrus (labeled 82, 84, 86, and 88) and 3275 voxels in the bilateral thalamus (labeled 231–246). We computed the vFC connectivity inference matrices $\mathbf{W}_{3566\times 1727}^{(\mathrm{Tem_{right}},\mathrm{Tha_{left}})}$ and $\mathbf{W}_{3566\times 1548}^{(\mathrm{Tem_{right}},\mathrm{Tha_{right}})}$ between clinical groups and then implemented SCCN. Due to limited space here, we provide the results of all estimated parameters and densely altered subarea pairs in Appendix D.3 (Lu et al. (2024)).

4. Simulations. In the simulation study, we probed whether SCCN can extract densely altered subarea pairs with better performance, compared to common existing methods. Specifically, we evaluated the performance from two perspectives: (i) Multivariate edge-level inference: whether extracted voxel pairs have a high true-positive rate (TPR) and low false-positive rate (FPR); (ii) network-level inference: whether the extracted subareas contain maximal true-positive voxels, compared to other unextracted subareas.

4.1. *Primary analysis.* We first generated a bipartite graph $G = \{U, V\}$ to represent the brain connectome between two brain regions A and B for S subjects, where U corresponds to the voxel set in Region A, and V corresponds to that in Region B. We assume all S subjects share a common set of nodes after spatial normalization and registration, that is, $(U^s, V^s) \equiv (U, V)$, $\forall s \in [S]$. Next, we simulated covariates of interest $\{\mathbf{X}^1, \ldots, \mathbf{X}^S\}$ that contain clinical

information of all S subjects. Lastly, we simulated the Fisher's z-transformation connectivity matrices $\{\mathbf{Z}^1, \ldots, \mathbf{Z}^S\}$ between regions A and B for all subjects, where $\mathbf{Z}^s \in \mathbb{R}^{n\times m}$, $n = |U|$, $m = |V|$. Specifically, each element z_{ij}^s in $\mathbf{Z}^s$ was set to follow $\mathcal{N}(h(z_{ij}^s), \sigma^2)$, where $h(z_{ij}^s) = \mathbf{X}^s \boldsymbol{\beta}_{ij}$ is location-specific within regions A and B.

In the following we show the numerical settings under the above simulation framework:

(i) For the two predefined brain regions of interest, we simulated $|U| = 900$ voxels in Region A and $|V| = 1600$ voxels in Region B. Within $|U|$ and $|V|$, we also randomly simulated three disease-related subarea pairs (U_1, V_1), (U_1, V_2), and (U_2, V_3). The true spatial locations of these five subareas in the simulated 2D grid spaces are presented in Figure 6(a1). Not every possible pair $\{(U_c, V_d), c = [2], d = [3]\}$ was associated with the disease; only regions with the same brightness exhibited dysconnectivity from A to B. The sizes of these subarea pairs were $|U_1||V_1| = 84 \times 70 = 5880$, $|U_1||V_2| = 84 \times 64 = 5376$, and $|U_2||V_3| = 96 \times 117 = 11{,}232$. In addition, we included spatially isolated abnormal voxels as well as noise within regions A and B to mimic more realistic neural connectivity (Figure 6(a2)).

(ii) For the Fisher's z-transformation connectivity matrices $\{\mathbf{Z}^s, s \in S\}$, we set $h(z_{ij}^s) = \beta_0 + \beta_{ij,1}x_1^s + \beta_{ij,2}x_2^s + \beta_{ij,3}x_3^s$, where x_1^s and x_2^s store the age and sex information for subject s, and x_3^s represents their clinical status ($x_3^s = 1$ if patient s has a mental disorder and 0 for a healthy control.). In addition, while $\beta_{ij,1}$ and $\beta_{ij,2}$ are typically not spatially variant, $\beta_{ij,3}$ is considered brain-region specific,

$$\beta_{ij,3} = \begin{cases} 0.9, & \text{if } (i,j) \in (U_1, V_1) \cup (U_1, V_2), \\ 0.13, & \text{if } (i,j) \in (U_2, V_3), \\ 0, & \text{if } (i,j) \in U/\{(U_1, V_1) \cup (U_1, V_2) \cup (U_2, V_3)\}. \end{cases}$$

(iii) To control standardized effect sizes, we set $\sigma^2 = 0.5, 1.0, 2.0$ in $\mathbf{Z}^s \sim \mathcal{N}(h(z_{ij}^s), \sigma^2)$. Additionally, four sample sizes, $S = 100$, 200, 2000, and 20,000, were used, each with balanced healthy controls and patients. All settings with different (σ, S) were simulated 1000 times to assess the variability of the TPR and FPR.

We implemented Algorithm 1 and 2 of SCCN to identify subarea pairs from each simulated dataset, and we then applied Algorithm 3 to conduct clusterwise inference on the subarea pairs detected. To assess the performance of the multivariate edgewise inference, we considered two conventional multiple-testing controls (FDR and FWER). Specifically, we used the voxelwise permutation test (with 1000 permutations) to control the FWER and the Benjamini–Hochberg procedure (with $q = 0.05$ as a cut-off) to control the FDR (Benjamini and Hochberg (1995)). To assess the accuracy of the clusterwise performance, our goal was to compare true disease-related subgraphs $\{(U_c, V_d)\}$ with the estimated subgraphs $\{(\widehat{U}_c, \widehat{V}_d)\}$ produced by five commonly used biclustering algorithms (i.e., Cheng and Church, Plaid, OPSM, xMOTIF, and Spectral Biclustering (Gupta, Singh and Verma (2013))).

The edgewise inference results are presented in Table 1, and a graph illustration of the results is shown in Figure 6. For the edgewise inference performance with all different (σ, S), SCCN outperforms the two traditional multiple testing correction methods (i.e., FDR and FWER control) in terms of TPR, while its ability to control the FPR falls in between the two. SCCN's relatively inferior performance in controlling the FPR (compared to sensitivity) can sometimes be impacted by the following disadvantage: in traditional multiple testing methods with universal thresholds, one false-positive finding corresponds to exactly one false-positive edge. However, SCCN detects altered edges by partitioning voxels within each ROI; therefore, one false-positive finding by SCCN corresponds to one false-positive voxel, say $v_i \in U_c$, which will lead to n false positive edges when V_d ($|V_d| = n$) is found to connect to $|U_c|$. The

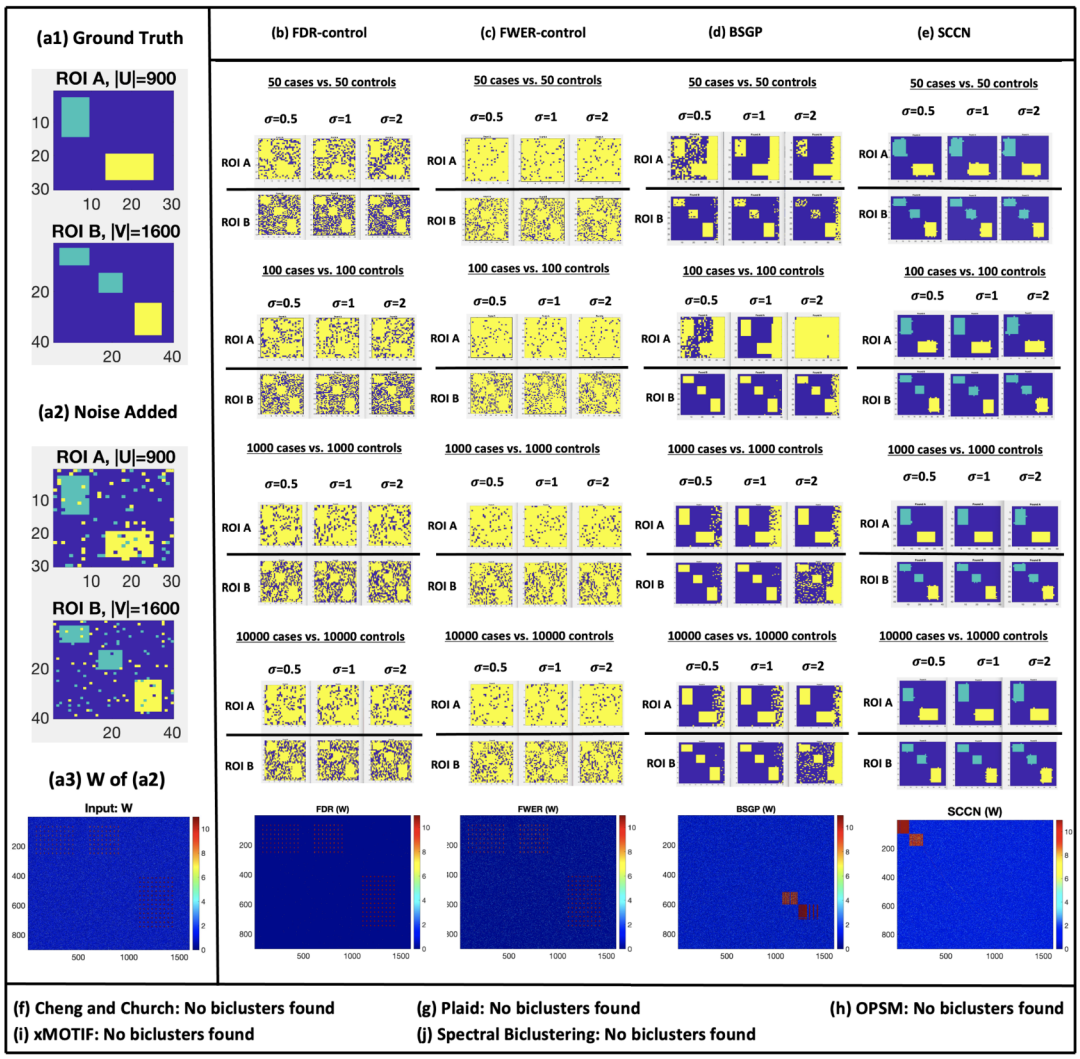

FIG. 6. *A 2D visualization of performance by different methods. In* (*a*1), *the true spatial locations of subareas* U_1 *and* U_2 *are displayed in a simulated* 30×30 *grid space while* V_1, V_2, *and* V_3 *are displayed in a simulated* 40×40 *grid space. Subareas with the same brightness contain disease-related edges from A to B, that is,* (U_1, V_1), (U_1, V_2), *and* (U_2, V_3) *are the positive subarea pairs.* (*a*2) *shows the scenario with false negative and false positive noises added to mimic the real vFC patterns in the brain connectome.* (*a*3) *shows the connectivity inference matrix* $\mathbf{W}$ *obtained based on* (*a*2). (*b*)–(*e*) *show the detected disease-related voxel pairs (again only regions with the same brightness form a pair) under different variances* σ *and sample sizes* S. *The last row shows the isomorphic graphs of* (*a*3) *with the extracted subarea pairs pushed to the top when* $\sigma = 1$. *We highlight the voxels from the suprathreshold voxel pairs that were yielded by the FDR-control and FWER-control along with voxels in subarea pairs that were extracted by BSGP and SCCN. Multiple testing with FDR-control and FWER-control tend to extract an excess of voxels with high false-positive error rates. BSGP better controls the error rates, but it extracts voxel pairs without differentiating the correct areawise connections, that is,* (U_1, V_1), (U_1, V_2), *and* (U_2, V_3). *In contrast, SCCN can simultaneously recover the spatially contiguous subareas, respectively, in A and B, and reveal the correct disease-related vFC patterns.* (*f*)–(*j*) *show that no single differentially expressed subarea pair was extracted by the biclustering algorithms listed.*

greater the size of V_d, the more false-positive edges will be yielded. Nonetheless, even with such a heavy penalty for detecting one false-positive voxel, SCCN still controls the FPR and shows better performance when jointly considering the TPR and FPR. More importantly, false-positive edges discovered by the traditional FDR and FWER correction approaches al-

TABLE 1

Simulation results. The four subtables show the inference results given different sample sizes and variances, where TPR and FPR correspond to the edgewise true positive rate and false positive rate. Network detection results indicate whether the algorithm can successfully extract the correct connection patterns between disease-related subarea pairs

Sample Size: 50 cases vs. 50 controls				
Methods	**σ**	**0.5**	**1**	**2**
FDR-control	TPR	0.918 (0.229)	0.832 (0.314)	0.637 (0. 328)
	FPR	0.060 (0.007)	0.065 (0.053)	0.073 (0.158)
	Network Detection	No	No	No
FWER-control	TPR	0.994 (0.169)	0.893 (0.177)	0.842 (0. 179)
	FPR	0.762 (0.142)	0.764 (0.152)	0.771 (0.193)
	Network Detection	No	No	No
SCCN	TPR	1(0)	1(0)	1(0)
	FPR	0.087 (0.011)	0.093 (0.012)	0.096 (0.014)
	Network Detection	Yes	Yes	Yes
BSGP	TPR	0.946 (0.106)	0.893 (0.122)	0.667 (0.278)
	FPR	0.858 (0.258)	0.773 (0.173)	0.845 (0.439)
	Network Detection	Yes	Yes	Yes
Cheng and Church Plaid OPSM xMOTIF Spectral Biclustering	TPR	0(0)	0(0)	0(0)
	FPR	0(0)	0(0)	0(0)
	Network Detection	No biclusters detected		

Sample Size: 100 cases vs. 100 controls				
Methods	**σ**	**0.5**	**1**	**2**
FDR-control	TPR	0.958 (0.215)	0.892 (0.249)	0.746 (0. 427)
	FPR	0.065 (0.069)	0.069 (0.048)	0.070 (0.164)
	Network Detection	No	No	No
FWER-control	TPR	0.994 (0.157)	0.989 (0.182)	0.842 (0. 163)
	FPR	0.767 (0.139)	0.762 (0.140)	0.761 (0.187)
	Network Detection	No	No	No
SCCN	TPR	1(0)	1(0)	1(0)
	FPR	0.081 (0.010)	0.082 (0.012)	0.097 (0.013)
	Network Detection	Yes	Yes	Yes
BSGP	TPR	1 (0.105)	1 (0.120)	0.993 (0.262)
	FPR	0.844 (0.228)	0.764 (0.172)	0.940 (0.369)
	Network Detection	Yes	Yes	Yes
Cheng and Church Plaid OPSM xMOTIF Spectral Biclustering	TPR	0(0)	0(0)	0(0)
	FPR	0(0)	0(0)	0(0)
	Network Detection	No biclusters detected		

Sample Size: 1000 cases vs. 1000 controls				
Methods	**σ**	**0.5**	**1**	**2**
FDR-control	TPR	0.957 (0.209)	0.878 (0.287)	0.789 (0. 363)
	FPR	0.061 (0.007)	0.061 (0.058)	0.071 (0.159)
	Network Detection	No	No	No
FWER-control	TPR	0.993 (0.169)	0.904 (0.180)	0.823 (0. 187)
	FPR	0.749 (0.140)	0.727 (0.145)	0.754 (0.176)
	Network Detection	No	No	No
SCCN	TPR	1(0)	1(0)	1(0)
	FPR	0.081 (0.008)	0.087 (0.010)	0.081 (0.012)
	Network Detection	Yes	Yes	Yes
BSGP	TPR	0.968 (0.106)	0.903 (0.122)	0.875 (0.278)
	FPR	0.374 (0.438)	0.405 (0.360)	0.737 (0.447)
	Network Detection	Yes	Yes	Yes
Cheng and Church Plaid OPSM xMOTIF Spectral Biclustering	TPR	0(0)	0(0)	0(0)
	FPR	0(0)	0(0)	0(0)
	Network Detection	No biclusters detected		

Sample Size: 10000 cases vs. 10000 controls				
Methods	**σ**	**0.5**	**1**	**2**
FDR-control	TPR	0.959 (0.229)	0.873 (0.357)	0.771 (0. 391)
	FPR	0.060 (0.007)	0.061 (0.061)	0.069 (0.160)
	Network Detection	No	No	No
FWER-control	TPR	0.992 (0.174)	0.907 (0.176)	0.819 (0. 183)
	FPR	0.753 (0.145)	0.734 (0.145)	0.759 (0.157)
	Network Detection	No	No	No
SCCN	TPR	1(0)	1(0)	1(0)
	FPR	0.081 (0.007)	0.091 (0.007)	0.087 (0.011)
	Network Detection	Yes	Yes	Yes
BSGP	TPR	0.972 (0.208)	0.884 (0.122)	0.873 (0.290)
	FPR	0.574 (0.426)	0.368 (0.499)	0.679 (0.407)
	Network Detection	Yes	Yes	Yes
Cheng and Church Plaid OPSM xMOTIF Spectral Biclustering	TPR	0(0)	0(0)	0(0)
	FPR	0(0)	0(0)	0(0)
	Network Detection	No biclusters detected		

most cover all within-ROI voxels, which leads to a substantial loss of spatial specificity when identifying covariate-related vFC patterns.

Regarding the network-level inference performance, all common biclustering methods failed to detect any positive biclusters (differentially expressed subarea pairs), except for BSGP. However, BSGP nonetheless failed to ensure spatial contiguity, and the precise connection between the extracted subareas was not correctly revealed. That is, unlike the results yielded by SCCN (Figure 6(e)), BSGP (Figure 6(d)) could not effectively differentiate between clusters with different levels of brightness. In comparison, SCCN shows outstanding network-level performance for detecting community structures and incorporating spatial contiguity.

4.2. *Negative control analysis*. We further performed a negative control analysis to evaluate the FPR of our method. We consider a scenario in which the connections between a preselected ROI pair are unrelated to a clinical condition of interest. We generated $|U| = 900$ and

$|V| = 1600$ voxels in regions A and B. We distinguished the patient and control groups as 1 and 0, but since there were no abnormal subarea pairs $\{(U_c, V_d)\}$ across groups, we simply set the connectivity matrices $\mathbf{Z}^s \sim \mathcal{N}(0, \sigma^2)$ over the entire regions for all S subjects. Based on $\mathbf{Z}^s$, we obtained the inference matrix $\mathbf{W^0}$ across clinical groups. Since the network detection was validated to be scalable to different sample sizes and sample variances, we evaluated the configuration ($S = 1000, \sigma = 1$) as a proof of concept. Finally, we implemented SCCN on $\mathbf{W^0}$. Since the false positive voxel pairs tended to be distributed randomly, no subarea pairs were significant. Therefore, the subarea-level false positive findings were 0. The edgewise FPR (suprathreshold voxel-pairs) among 1000 iterations was 6.82×10^{-5}(std. 1.29×10^{-5}), which is consistent with the predetermined alpha level ($\mathbb{E}(p) = 0.00005$). We have provided a graph visualization of these results in Appendix F (Lu et al. (2024)).

In summary, we have shown that the subarea detection is not affected by different values of variance σ^2, sample size S, or other sources of noise. SCCN also yields vFC patterns with high sensitivity and low FPRs. The spatial-contiguity constraints allow positive edges to borrow strengths from each other within a data-driven subarea; sensitivity is thus notably increased. Data-driven subareas with these constraints can also exclude false-positive edges that bridge voxels that are randomly scattered in ROIs. False-positive findings are, therefore, largely suppressed. In addition, the jointly improved sensitivity (and thus statistical power) and control of the FPR yield almost identical voxel sets across all simulated datasets. Replicability is hence remarkably improved.

5. Discussion. Psychiatric and neurological disorders are often associated with a disrupted brain connectome. To improve the spatial specificity and sensitivity for detecting a disease-impacted brain connectome, in this work we focused on voxel-level connectivity network analysis. We developed statistical models focusing on extracting abnormal voxel pairs from a region pair of interest, which can be further extended to whole-brain connectome analysis. We have attempted to simultaneously address the challenges of a controlled FPR for multiple voxel-pair testing and the spatial-contiguity constraints for vFC analysis.

In addition, the brain parcellation to extract subareas is usually based on commonly used brain atlases (e.g., Brodmann's map or the International Consortium for Brain Mapping), and these were built on comprehensively studied cortical anatomy, such as complex gyro-sulcal folding patterns. Different regions blocked by gyri and sulci tend to show differential neurobiological structures and functions, and these atlases can thus serve as a good foundation to investigate subarea community structures. However, to further overcome the limitation of using existing brain parcellations, one can consider combining any extracted spatially adjacent subareas from a pair of spatially adjacent regions if the combination is statistically coherent and biologically meaningful.

The centerpiece of our proposed method is the identification of subarea pairs containing an unusually high density of phenotype-related voxel pairs. By leveraging this high density, we can effectively control the FPR by excluding isolated false-positive edges, and we thus greatly reduce the number of false-positive nodes. We have, therefore, improved the spatial specificity of extracted disease-related patterns at a voxel level. Herein, we have proposed a new nonparametric objective function to achieve this goal, and this has been implemented with efficient algorithms. We also developed inference methods to assess the statistical significance of each subarea pair extracted.

The biological findings from our data example are novel; SCCN revealed vFC connectome patterns for schizophrenia within the well-known salience network. We discovered that the malfunction of salience network connectivity is mainly driven by disrupted connections between the dorsal insula and anterior cingulate cortex, instead of the omnibus region-level findings. We further validated our findings through extensive simulations and showed that our methods could improve sensitivity with a controlled FPR while retaining spatial contiguity.

In summary, SCCN provides a new toolkit for vFC analysis with improved spatial resolution and specificity while preserving a well-controlled false-positive error rate. Therefore, the findings from SCCN can be translated into more effective potential treatments for brain disorders. Since the input data of SCCN is voxel-pair-level inference results, it is applicable to all connectivity measures and data modalities where valid statistical inference can be performed (e.g., white-matter tractography). SCCN may also provide a promising strategy for whole-brain connectome voxel-pair network analysis. All sample code can be found at https://github.com/TongLu-bit/DecodingNetwork-SCCN.

Funding. The research work of Tong Lu and Shuo Chen was supported by the National Institute on Drug Abuse of the National Institutes of Health under Award Number 1DP1DA048968-01.

Yuan Zhang's research was supported by the Division of Mathematical Sciences of the National Science Foundation under Number 2311109.

SUPPLEMENTARY MATERIAL

Appendix (DOI: 10.1214/23-AOAS1824SUPPA; .pdf). The appendix provides supplementary details on the following topics: (i) definition and implementation of spatial-contiguity constraints; (ii) within-region vFC association analysis; (iii) proofs of Lemma 1 and Theorem 1 & 2, and construction of the MDL-based test statistics; (iv) additional information on the schizophrenia data analysis; (v) additional information on UK Biobank smoking data analysis; (vi) additional information on negative control analysis.

Code for implementing SCCN model (DOI: 10.1214/23-AOAS1824SUPPB; .zip). This supplementary file contains MATLAB codes to implement algorithms proposed in this paper.

REFERENCES

AGOSTA, F., SALA, S., VALSASINA, P., MEANI, A., CANU, E., MAGNANI, G., CAPPA, S. F., SCOLA, E., QUATTO, P. et al. (2013). Brain network connectivity assessed using graph theory in frontotemporal dementia. *Neurology* **81** 134–143.

ARNOLD, S. E. and TROJANOWSKI, J. Q. (1996). Recent advances in defining the neuropathology of schizophrenia. *Acta Neuropathol*. **92** 217–231. https://doi.org/10.1007/s004010050512

BAHRAMI, M., LAURIENTI, P. J. and SIMPSON, S. L. (2019). Analysis of brain subnetworks within the context of their whole-brain networks. *Hum. Brain Mapp*. **40** 5123–5141. https://doi.org/10.1002/hbm.24762

BENJAMINI, Y. and HOCHBERG, Y. (1995). Controlling the false discovery rate: A practical and powerful approach to multiple testing. *J. Roy. Statist. Soc. Ser. B* **57** 289–300. MR1325392

BULLMORE, E. and SPORNS, O. (2009). Complex brain networks: Graph theoretical analysis of structural and functional systems. *Nat. Rev. Neurosci*. **10** 186–198. https://doi.org/10.1038/nrn2575

CAO, M., WANG, J.-H., DAI, Z.-J., CAO, X.-Y., JIANG, L.-L., FAN, F.-M., SONG, X.-W., XIA, M.-R., SHU, N. et al. (2014). Topological organization of the human brain functional connectome across the lifespan. *Dev. Cogn. Neurosci*. **7** 76–93.

ÇETIN, M. S., CHRISTENSEN, F., ABBOTT, C. C., STEPHEN, J. M., MAYER, A. R., CAÑIVE, J. M., BUSTILLO, J. R., PEARLSON, G. D. and CALHOUN, V. D. (2014). Thalamus and posterior temporal lobe show greater inter-network connectivity at rest and across sensory paradigms in schizophrenia. *NeuroImage* **97** 117–126. https://doi.org/10.1016/j.neuroimage.2014.04.009

CHEN, S., BOWMAN, F. D. and MAYBERG, H. S. (2016). A Bayesian hierarchical framework for modeling brain connectivity for neuroimaging data. *Biometrics* **72** 596–605. MR3515786 https://doi.org/10.1111/biom.12433

CRADDOCK, R. C., JAMES, G. A., HOLTZHEIMER III, P. E., HU, X. P. and MAYBERG, H. S. (2012). A whole brain fMRI atlas generated via spatially constrained spectral clustering. *Hum. Brain Mapp*. **33** 1914–1928.

DERADO, G., BOWMAN, F. D. and KILTS, C. D. (2010). Modeling the spatial and temporal dependence in fMRI data. *Biometrics* **66** 949–957. MR2758231 https://doi.org/10.1111/j.1541-0420.2009.01355.x

EFRON, B. (2010). *Large-Scale Inference*: *Empirical Bayes Methods for Estimation*, *Testing*, *and Prediction*. *Institute of Mathematical Statistics* (*IMS*) *Monographs* **1**. Cambridge Univ. Press, Cambridge. MR2724758 https://doi.org/10.1017/CBO9780511761362

EICKHOFF, S. B., THIRION, B., VAROQUAUX, G. and BZDOK, D. (2015). Connectivity-based parcellation: Critique and implications. *Hum. Brain Mapp.* **36** 4771–4792. https://doi.org/10.1002/hbm.22933

ERSCHE, K. D., BARNES, A., JONES, P. S., MOREIN-ZAMIR, S., ROBBINS, T. W. and BULLMORE, E. T. (2011). Abnormal structure of frontostriatal brain systems is associated with aspects of impulsivity and compulsivity in cocaine dependence. *Brain* **134** 2013–2024.

FAN, J., HAN, X. and GU, W. (2012). Estimating false discovery proportion under arbitrary covariance dependence. *J. Amer. Statist. Assoc.* **107** 1019–1035. MR3010887 https://doi.org/10.1080/01621459.2012.720478

FAN, J. and LV, J. (2008). Sure independence screening for ultrahigh dimensional feature space. *J. R. Stat. Soc. Ser. B. Stat. Methodol.* **70** 849–911. MR2530322 https://doi.org/10.1111/j.1467-9868.2008.00674.x

FAN, L., LI, H., ZHUO, J., ZHANG, Y., WANG, J., CHEN, L., YANG, Z., CHU, C., XIE, S. et al. (2016). The human brainnetome atlas: A new brain atlas based on connectional architecture. *Cereb. Cortex* **26** 3508–3526.

FEDOTA, J. R. and STEIN, E. A. (2015). Resting-state functional connectivity and nicotine addiction: Prospects for biomarker development. *Ann. N.Y. Acad. Sci.* **1349** 64–82. https://doi.org/10.1111/nyas.12882

FERRI, J., FORD, J., ROACH, B., TURNER, J., VAN ERP, T., VOYVODIC, J., PREDA, A., BELGER, A., BUSTILLO, J. et al. (2018). Resting-state thalamic dysconnectivity in schizophrenia and relationships with symptoms. *Psychol. Med.* **48** 2492–2499.

FORNITO, A., ZALESKY, A. and BULLMORE, E. (2016). *Fundamentals of Brain Network Analysis*. Academic Press, San Diego.

GAZNICK, N., TRANEL, D., MCNUTT, A. and BECHARA, A. (2014). Basal ganglia plus insula damage yields stronger disruption of smoking addiction than basal ganglia damage alone. *Nicotine Tob. Res.* **16** 445–453. https://doi.org/10.1093/ntr/ntt172

GRÜNWALD, P. D. (2007). *The Minimum Description Length Principle*. MIT Press, Cambridge.

GUPTA, J. K., SINGH, S. and VERMA, N. K. (2013). MTBA: MATLAB Toolbox for Biclustering Analysis. 94-97. IEEE.

KAMVAR, S., KLEIN, D. and MANNING, C. (2003). Spectral Learning Technical Report No. 2003-25 Stanford InfoLab.

LI, R., ZHONG, W. and ZHU, L. (2012). Feature screening via distance correlation learning. *J. Amer. Statist. Assoc.* **107** 1129–1139. MR3010900 https://doi.org/10.1080/01621459.2012.695654

LOEWE, K., GRUESCHOW, M., STOPPEL, C. M., KRUSE, R. and BORGELT, C. (2014). Fast construction of voxel-level functional connectivity graphs. *BMC Neurosci.* **15** 1–13.

LU, T., ZHANG, Y., KOCHUNOV, P., HONG, E. and CHEN, S. (2024). Supplement to "Network method for voxel-pair-level brain connectivity analysis under spatial-contiguity constraints." https://doi.org/10.1214/23-AOAS1824SUPPA, https://doi.org/10.1214/23-AOAS1824SUPPB

LYNALL, M.-E., BASSETT, D. S., KERWIN, R., MCKENNA, P. J., KITZBICHLER, M., MULLER, U. and BULLMORE, E. (2010). Functional connectivity and brain networks in schizophrenia. *J. Neurosci.* **30** 9477–9487. https://doi.org/10.1523/JNEUROSCI.0333-10.2010

MCCLERNON, F. J., CONKLIN, C. A., KOZINK, R. V., ADCOCK, R. A., SWEITZER, M. M., ADDICOTT, M. A., CHOU, Y.-H., CHEN, N.-K., HALLYBURTON, M. B. et al. (2016). Hippocampal and insular response to smoking-related environments: Neuroimaging evidence for drug-context effects in nicotine dependence. *Neuropsychopharmacology* **41** 877–885.

NICHOLS, T. E. and HOLMES, A. P. (2002). Nonparametric permutation tests for functional neuroimaging: A primer with examples. *Hum. Brain Mapp.* **15** 1–25. https://doi.org/10.1002/hbm.1058

PALANIYAPPAN, L., WHITE, T. P. and LIDDLE, P. F. (2012). The concept of salience network dysfunction in schizophrenia: From neuroimaging observations to therapeutic opportunities. *Curr. Top. Med. Chem.* **12** 2324–2338. https://doi.org/10.2174/156802612805289881

ROGERS, B. P., MORGAN, V. L., NEWTON, A. T. and GORE, J. C. (2007). Assessing functional connectivity in the human brain by fMRI. *Magn. Reson. Imaging* **25** 1347–1357. https://doi.org/10.1016/j.mri.2007.03.007

RUBINOV, M. and SPORNS, O. (2010). Complex network measures of brain connectivity: Uses and interpretations. *NeuroImage* **52** 1059–1069. https://doi.org/10.1016/j.neuroimage.2009.10.003

SIMPSON, S. L., BOWMAN, F. D. and LAURIENTI, P. J. (2013). Analyzing complex functional brain networks: Fusing statistics and network science to understand the brain. *Stat. Surv.* **7** 1–36. MR3161730 https://doi.org/10.1214/13-SS103

SUTHERLAND, M. T. and STEIN, E. A. (2018). Functional neurocircuits and neuroimaging biomarkers of tobacco use disorder. *Trends Mol. Med.* **24** 129–143. https://doi.org/10.1016/j.molmed.2017.12.002

THIRION, B., FLANDIN, G., PINEL, P., ROCHE, A., CIUCIU, P. and POLINE, J.-B. (2006). Dealing with the shortcomings of spatial normalization: Multi-subject parcellation of fMRI datasets. *Hum. Brain Mapp.* **27** 678–693. https://doi.org/10.1002/hbm.20210

WIG, G. S., LAUMANN, T. O. and PETERSEN, S. E. (2014). An approach for parcellating human cortical areas using resting-state correlations. *NeuroImage* **93** 276–291. https://doi.org/10.1016/j.neuroimage.2013.07.035

WU, G.-R., STRAMAGLIA, S., CHEN, H., LIAO, W. and MARINAZZO, D. (2013). Mapping the voxel-wise effective connectome in resting state fMRI. *PLoS ONE* **8** e73670.

WU, T., WANG, L., HALLETT, M., CHEN, Y., LI, K. and CHAN, P. (2011). Effective connectivity of brain networks during self-initiated movement in Parkinson's disease. *NeuroImage* **55** 204–215.

WYLIE, K. P. and TREGELLAS, J. R. (2010). The role of the insula in schizophrenia. *Schizophr. Res*. **123** 93–104. https://doi.org/10.1016/j.schres.2010.08.027

XIA, Y. and LI, L. (2017). Hypothesis testing of matrix graph model with application to brain connectivity analysis. *Biometrics* **73** 780–791. MR3713112 https://doi.org/10.1111/biom.12633

XIA, Y. and LI, L. (2019). Matrix graph hypothesis testing and application in brain connectivity alternation detection. *Statist*. *Sinica* **29** 303–328. MR3889369